Hybrid Lattice Boltzmann Method for Turbulent Non-Ideal Compressible Fluid Dynamics

Lucien Vienne, Alexis Giauque, Emmanuel Lévêque

Hybrid Lattice Boltzmann Method for Turbulent Non-Ideal Compressible Fluid Dynamics

Lucien Vienne,[a] Alexis Giauque, and Emmanuel Lévêque
CNRS, Ecole Centrale de Lyon, INSA Lyon, Universite Claude Bernard Lyon 1, LMFA, UMR5509, 69134 Écully, France

The development and application of a compressible hybrid lattice Boltzmann method to high Mach number supercritical and dense gas flows are presented. Dense gases, especially in Organic Rankine Cycle turbines, exhibit non-classical phenomena that offer the possibility of enhancing turbine efficiency by reducing friction drag and boundary layer separation. The proposed numerical framework addresses the limitations of conventional lattice Boltzmann method in handling highly compressible flows by integrating a finite-volume scheme for the total energy alongside a non-ideal gas equation of state supplemented by a transport coefficient model. Validations are performed using a shock tube and a three-dimensional Taylor-Green vortex flow. The capability to capture non-classical shock behaviors and compressible turbulence is demonstrated. Our study gives the first analysis of a turbulent Taylor-Green vortex flow in a dense Bethe-Zel'dovich-Thompson gas and provides comparisons with perfect gas flow at equivalent Mach numbers. The results highlight differences associated with dense gas effects and contribute to a broader understanding of non-ideal fluid dynamics in engineering applications.

Keywords: lattice Boltzmann method; non-ideal compressible fluid dynamics; dense gas; shock tube; Taylor-Green vortex

I. INTRODUCTION

Waste heat recovery or heat harvesting from geothermal reservoirs represents a promising way of generating emissions-free power. To achieve this, one of the preferred technical solutions has been known for the last 50 years and is named after the thermodynamic cycle that it uses to convert heat into recoverable work (such as electricity): the Organic Rankine Cycle (ORC). ORC uses an organic fluid instead of water in a steam turbine cycle. Because of the moderate boiling temperature of the organic fluid (such as siloxane), new heat sources such as waste heat in industry can be harvested. A major challenge in ORC systems is to enhance the overall efficiency of the cycle to get as close as possible to the Carnot limit imposed by the laws of thermodynamics, i.e. $\eta_\infty = 1 - T_{\text{cold}}/T_{\text{hot}}$ where T_{cold} and T_{hot} denote the temperatures of the cold and warm sources, respectively. The overall efficiency results from the combined optimization of all sub-elements that make up the cycle. One of the most important sub-system is the turbine stage in which the fluid undergoes a very strong expansion creating shock-waves and large turbulence levels.

The working fluids used in ORC systems usually have a high molecular complexity. Such fluids are particularly suitable because of their high heat capacity and low boiling temperature. They also often exhibit strong non-ideal behaviors when their thermodynamic state is close to the critical point[1]. In this region of the $p - v$ diagram, the so-called fundamental derivative of gas dynamics can become lower than unity ($\Gamma < 1$), which leads to some unusual behaviors[2], such as expansion shock-waves or composite waves. The term "fundamental" here underlines the importance of Γ in determining the non-linear behavior of the gas. The fundamental derivative of gas dynamics was introduced by Hayes[3] and later

[a]Corresponding author: contact@lvienne.com

rewritten by Thompson[2] as

$$\Gamma = \frac{v^3}{2c^2}\frac{\partial^2 p}{\partial v^2}\bigg|_s = \frac{c^4}{2v^3}\frac{\partial^2 v}{\partial p^2}\bigg|_s = 1 + \frac{\rho}{c}\frac{\partial c}{\partial \rho}\bigg|_s \tag{1}$$

where v denotes the specific volume, ρ is the mass density, $c = \sqrt{\partial p/\partial \rho|_s}$ defines the speed of sound, p is the pressure and s is the entropy of the fluid. According to its definition (1), Γ may be viewed as a measure of the rate of change of the speed of sound during an isentropic transformation. It is also directly related to the curvature of isentropic lines in the $p-v$ diagram, i.e. $\partial^2 p/\partial v^2|_s$. In general, three main regimes can be identified according to the value of the fundamental derivative Γ (see Fig. 6 later):

- $\Gamma > 1$ corresponds to a classical ideal (perfect) gas behavior. Let us mention that for thermally and calorically perfect gases, the constant fundamental derivative is expressed as $\Gamma = (\gamma+1)/2$ with γ denoting the heat capacity ratio.
- $0 < \Gamma < 1$ is specific to the classical non-ideal gas behavior. In this regime, the speed of sound decreases in isentropic compressions, $\partial c/\partial \rho|_s < 0$.
- $\Gamma < 0$ is particularly interesting and indicates the presence of non-classical non-ideal gas behavior also known as Bethe-Zel'dovich-Thompson (BZT) effect. The name BZT was given by Cramer[4] to acknowledge the pioneering works of Bethe[5], Zel'dovich[6] and Thompson[2] on dense gases, since widely used in the industry. Hydrocarbons, perfluorocarbons, and siloxanes are examples of such BZT gases. In the $p-v$ diagram, it corresponds to a limited region where the negative sign of the fundamental derivative allows the (unusual) development of expansion shock-waves (see Fig. 6).

Several studies examined the non-classical phenomena occurring in dense BZT gases (such as expansion shock-waves) by considering at first the fluid as inviscid[7–12]. Adding viscosity effects allowed the study of boundary layers and the interaction between shocks and boundary layers[13–16]. The benefits of using dense gases in ORC turbines were demonstrated when operating within the region $0 < \Gamma < 1$ at transonic speeds. Under these conditions, dense gas effects minimize friction drag and boundary layer separation[17]. When the expansion occurs within the inversion region $\Gamma < 0$, the shock intensity decreases and entropy losses are reduced, improving the efficiency of the turbine.

For years, the efficiency of ORC systems has been addressed through in situ optimization. Meanwhile, modern numerical simulation and design tools for non-ideal fluids have emerged in the turbomachinery field. Therefore, techniques originally developed for ideal flows have been effectively applied to optimize components operating under non-ideal flow conditions, such as supersonic vanes in ORC turbines, with Vitale et al.[18] employing automatic differentiation tools to develop adjoint Non-Ideal Compressible Fluid Dynamics (NICFD) solvers, albeit facing challenges with external thermodynamic property libraries as noted by Rubino et al.[19]. The evaluation of geometrical uncertainties was initially explored by Razaaly et al.[20], while shape optimization under uncertainty, encompassing operating conditions and model parameters, was pioneered by Cinnella and Hercus[21]. A recent review by Guardone et al.[1] reports a comprehensive theoretical framework embedding the fundamentals of NICFD.

However, one of the main obstacles to using simulations for the optimal design of ORC turbines is the "time to result". To date, only high-fidelity techniques[22–24] have achieved the requested level of accuracy, but are also too time-consuming to be integrated into a real-time shape optimization task. The "time to result" for industrial applications involving complex boundaries is primarily determined by two factors: grid generation and the efficiency of solver algorithms. Implementing a Cartesian octree grid along with immersed boundary conditions for wall-modeled large eddy simulation has drastically reduce grid generation time from 1-2 months to 1-2 hours in the case of aircraft high-lift devices[25]. Based on a Cartesian grid, the lattice Boltzmann method (LBM) provides a relatively simple and efficient core algorithm that is also easy to parallelize. These advantages can lead to speed-ups of up to ten times compared to traditional Navier-Stokes solvers in industrial

large eddy simulations, including applications in landing gears aeroacoustics[26–28], aircraft high-lift devices[29,30], automotive aerodynamics[31], and reacting flows[32]. While no equivalent comparison with traditional Navier-Stokes solvers is available for turbo-machinery flows, recent studies[33–35] demonstrate the adoption of the LBM in turbo-machine flow simulations. Exploiting the LBM to tackle compressible turbulent flows of a non-ideal fluid would represent a first step in efficient optimal design of ORC turbines.

The LBM is a fully discretized (in space, time, and velocity) kinetic approach that originates from the Lattice Gas Automata method, first introduced in 1973 by Hardy et al.[36]. It may be interpreted as a minimalist statistical model, where populations of particles move simultaneously along a regular lattice, following simple rules of streaming and collision from which macroscopic dynamics emerges naturally. The method gained momentum in the computational-fluid-dynamics community after the publication of the so-called lattice-BGK model in 1992[37,38], in which the collision was simplified to a relaxation towards a local equilibrium, and the consistency with the Navier–Stokes dynamics made explicit. Although historically introduced in the context of dilute gas dynamics, the method was rapidly extended to encompass more complex dynamics[39].

The LBM algorithm faces challenges when simulating highly compressible flows. Indeed, the drastic decimation of the (microscopic) velocity space generates errors that increase with the Mach number, which limits its application to weakly compressible flows at low speed. This can a priori be overcome by extending the discrete set of microscopic velocities[40–44], but this entails a tremendous expansion of the spatial stencil of the method, resulting in an increased algorithmic complexity, greater memory requirements, and difficulties in maintaining numerical stability[45]. To enhance the applicability of the LBM to thermal, compressible, and reactive flows, a hybrid approach combining an LBM algorithm for the fluid momentum with a finite-difference or finite-volume algorithm for the total energy, has recently been proposed. This approach uses the same grid and time step for both discretization schemes, providing a unified solution that has proven efficient, as demonstrated by Feng et al.[46] and Boivin et al.[32]. These recent advances open new opportunities for the simulation of realistic ORC systems, with an additional need to implement equations of state (EOS) for non-ideal dense gas thermodynamic conditions. This later aspect has recently been examined by Hosseini et al.[47], focusing mainly on the added complexity of the van der Walls' EOS and applying their developments to phase-transition problems. Non-ideal compressible fluid dynamics in a turbulent regime has yet to be addressed.

In this context, our main objective is twofold. Firstly, to introduce a compressible hybrid-LBM approach encompassing a third-order EOS and, secondly, to apply it to study for the first time the dense and BZT effects in the well-known Taylor-Green Vortex (TGV) flow. The article is organized as follows. First, a new hybrid-LBM scheme is described, which is capable of handling turbulent dense gas flows. A focus is made on the specific aspects related to the energy equation, the implementation of the third-order Peng-Robinson EOS[48] and the transport coefficient model introduced by Chung[49]. Results for highly compressible flows of dense gases are validated against the literature in the second section. The third section further validates the method by examining the TGV flow in a supersonic perfect gas and then extends the analysis to a dense BZT gas. The TGV configuration is usually considered a benchmark in turbulence simulations. This is the first time it has been analyzed in the context of dense gases. This paper compares the results with the ideal gas flow at the same turbulent Mach number and reports the differences found. The final section summarizes the main findings and provides a roadmap for further research.

II. NON-IDEAL GAS MODELING IN HYBRID COMPRESSIBLE LATTICE BOLTZMANN

The LBM stems from the Boltzmann equation and can be considered a kinetic method. Using a kinetic approach to simulate continuum flows may seem unreasonable at first glance, but it has several advantages. Firstly, the velocity space is amenable to a radical reduction so that only a small set of microscopic (or kinetic) velocities, e.g. nine in two dimensions, is

sufficient to reconstruct relevant isothermal fluid dynamics at the macroscopic level (with a third-order error in Mach number). The most important feature of the LBM is certainly that its kinetic equations dissociate non-locality and non-linearity, thus facilitating numerical integration. As a result, the so-called *stream-and-collide* algorithm is simple, accurate, and formidably efficient in terms of computations. The applications of the LBM are now numerous in both academic and industrial configurations, and extend to a much wider scope than the initial domain of weakly compressible dynamics of ideal gases[50–53].

Simulating compressible non-ideal gas dynamics using the LBM involves two major challenges: (i) handling strong compressibility effects associated with high density and pressure gradients, and (ii) incorporating thermodynamic relations including a thermal and a caloric EOS for the pressure and the internal energy, i.e. $p(\rho, T)$ and $e(\rho, T)$.

(i) Significant progress has been made in addressing compressibility in the LBM. The *multi-speed* approach[40–44] was introduced to include third-order statistical moments (related to heat exchanges) in the dynamics. However, this comes at the cost of an increase in the number of microscopic velocities, which also implies more difficulties in implementing boundary conditions and ensuring stability[45]. Alternatively, the *off-lattice* method uses an adaptive (microscopic) velocity space that directly accounts for compressibility effects. This approach ensures Galilean invariance and is thermodynamically consistent, but it requires interpolations to redistribute particles onto a fixed lattice at each time step[54,55], which compromises mass conservation and increases significantly the computational costs. In addition, it is usually combined with *multi-speed* strategy to mitigate the Mach number error. Despite these drawbacks, the *off-lattice* method is based on solid physical grounds and has recently proven its effectiveness[56]. Another method for simulating compressible flows involves solving the density and momentum equations with the standard LBM scheme, while the energy equation is handled separately, possibly using a different scheme. This splitting leads to the *double-distribution-function* approach when the energy equation is addressed using a second LBM scheme[57,58]. This method is limited to weakly compressible thermal flows, unless it is enhanced by the *multi-speed* or *off-lattice* approach. The *hybrid* approach, on the other hand, relies on a conventional finite-volume or finite-difference scheme to solve the energy equation.[59]. This strategy will be continued in the following. Coupling two distinct numerical schemes is always challenging when it comes to stability. For this reason, the entropy was first chosen as the base variable for the energy equation. As a characteristic variable of the Euler equations, this choice guarantees that the energy scheme can remain linearly decoupled from the lattice Boltzmann (LB) scheme. More recently Wissocq et al.[60] proposed a robust and stable compressible *hybrid* LB approach based on a total energy formulation[60,61] to restore missing conservation features in the previous *hybrid* entropy-based approach. Let us mention that Guo and Feng[62] have recently introduced an alternative strategy for coupling LB and finite-volume schemes.

(ii) Regarding non-ideal thermodynamics, LB solvers have introduced various strategies to go beyond the perfect gas EOS, in particular in the context of multi-phase flows. However, these methods are generally limited to weakly compressible flows, making stable and accurate simulations of compressible flows difficult. Notable exceptions are the works of Reyhanian et al.[56,63], who used the so-called *particle-on-demand* scheme — an advanced *off-lattice* approach — in conjunction with the van der Waals equation of state and the assumption of a calorically perfect gas.

In the following section, an extension of the work[59,60] is built up to include arbitrary non-ideal thermal and caloric equations of state, opening up the *hybrid* LBM approach to general non-ideal compressible fluid dynamics.

A. Lattice Boltzmann scheme for mass and momentum

The LBM governs the evolution in time of the distribution functions $(f_0, \cdots, f_{N-1})$ of particles with the microscopic velocities $(\boldsymbol{e}_0, \cdots, \boldsymbol{e}_{N-1})$ at each lattice node. At the macroscopic level, flow variables are recovered by summing the contributions from the distribution

functions and calculating the moments so that

$$\rho = \sum_{i=0}^{N-1} f_i \quad \text{and} \quad \rho u_\alpha = \sum_{i=0}^{N-1} f_i e_{i\alpha}, \tag{2}$$

where ρ and u_α represent respectively the mass density and velocity components of the fluid. The truncation of the velocity space onto a finite basis of Hermite polynomials and resorting to Gaussian quadrature formula[40,64] transform the Boltzmann equation to the discrete-velocity Boltzmann equation. Our study truncates the velocity space to the standard D3Q27 lattice, i.e. $N = 27$ distribution functions in three dimensions. This stencil encompasses all the adjacent nodes in the uniform Cartesian grid as pictured in Fig. 1.

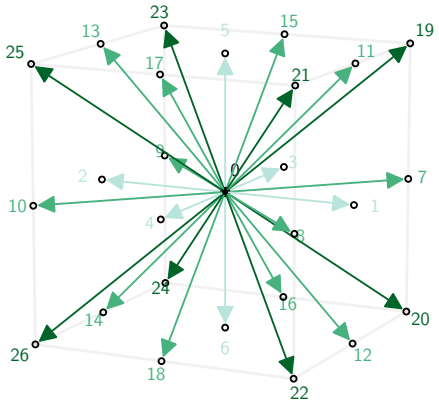

FIG. 1: Sketch of the D3Q27 stencil. The current node is the black-filled circle at the center. Neighboring nodes are drawn as black non-filled circles. D3Q27 distribution functions are related to the kinetic velocities represented by all possible permutations of $e_{i\alpha} = 0, -1, +1$ for $i = 0, \ldots, 26$ and $\alpha = x, y, z$.

The discretization in space and time involves the integration along the characteristics and results in the lattice Boltzmann scheme, a two-step algorithm that consists of

$$f_i^{coll}(t, \boldsymbol{x}) = f_i^{eq}(t, \boldsymbol{x}) + \left(1 - \frac{\Delta t}{\tau}\right) f_i^{neq}(t, \boldsymbol{x}) + \frac{\Delta t}{2} S_i(t, \boldsymbol{x}) + \Delta t F_i^{\mu_b}(t, \boldsymbol{x}) \qquad \text{collision step,} \tag{3}$$

$$f_i(t + \Delta t, \boldsymbol{x}) = f_i^{coll}(t, \boldsymbol{x} - \boldsymbol{e}_i \Delta t) \qquad \text{streaming step,} \tag{4}$$

for $i = 0, \cdots, 26$. Usual notations for the LB scheme are employed. τ denotes the relaxation time toward the equilibrium distribution function f_i^{eq}. S_i refers to the source term, and the non-equilibrium component is defined as

$$f_i^{neq} = f_i - f_i^{eq} + \frac{1}{2} \Delta t S_i \tag{5}$$

Following Farag et al.[59] but leaving the EOS $p(\rho, T)$ undefined, the equilibrium distribution is a third-order Hermite polynomials expansion

$$f_i^{eq} = w_i \rho \left[1 + \frac{e_{i\alpha}}{c_s^2} u_\alpha + \frac{H_{i\alpha\beta}}{2c_s^4} u_\alpha u_\beta + \frac{H_{i\alpha\beta\gamma}}{6c_s^6} u_\alpha u_\beta u_\gamma\right] + d_i \tag{6}$$

with

$$d_{i\neq 0} = \frac{w_i}{c_s^2}\left(p - \rho c_s^2\right) \quad \text{and} \quad d_{i=0} = \frac{w_0 - 1}{c_s^2}\left(p - \rho c_s^2\right), \tag{7}$$

where implicit (Einstein) summation is assumed over space coordinates $\alpha, \beta, \gamma \in \{x, y, z\}$, and d_i is a scalar that accounts for the deviation from the perfect gas assumption in the equivalent macroscopic equations. This operator is more isotropic and is known to be more stable than a conventional third-order Hermite polynomials expansion of the equilibrium function[65–67]. Expressions of the Hermite polynomials are given in Appendix A.

The general formulation of the source term reads

$$S_i = w_i(\dot{m} + \frac{H_{i\alpha}}{c_s^2}\rho F_\alpha + \frac{H_{i\alpha\beta}}{2c_s^4}\mathrm{Corr}_{\alpha\beta}) \tag{8}$$

where $\dot{m}$ is a mass source term, F_α is a body force, and $\mathrm{Corr}_{\alpha\beta}$ are second-order correction terms that are detailed later. Let us mention that correction terms should a priori depend on $\dot{m}$ and F_α. In the following, we will assume that there is no mass source term $\dot{m} = 0$ nor body force $F_\alpha = 0$, and that $\mathrm{Corr}_{\alpha\beta}$ corrects intrinsic errors arising from the discretization of the velocity space.

Macroscopic quantities are derived from the statistical moments of the distribution functions. Besides Eq. (2), the second and third-order moments of the distribution functions are designated by

$$\Pi_{\alpha\beta} = \sum_i e_{i\alpha} e_{i\beta} f_i, \tag{9}$$

$$\Pi_{\alpha\beta\gamma} = \sum_i e_{i\alpha} e_{i\beta} e_{i\gamma} f_i. \tag{10}$$

Similarly, the moments of the equilibrium state gives

$$\rho = \sum_i f_i^{eq}, \tag{11}$$

$$\rho u_\alpha = \sum_i e_{i\alpha} f_i^{eq} \tag{12}$$

$$\Pi_{\alpha\beta}^{eq} = \sum_i e_{i\alpha} e_{i\beta} f_i^{eq} = \rho u_\alpha u_\beta + \delta_{\alpha\beta} p, \tag{13}$$

$$\Pi_{\alpha\beta\gamma}^{eq,theo} = \rho u_\alpha u_\beta u_\gamma + \rho c_s^2 [u\delta]_{\alpha\beta\gamma} \tag{14}$$

where $[u\delta]_{\alpha\beta\gamma}$ stands for a cyclic permutation $[u\delta]_{\alpha\beta\gamma} = u_\alpha \delta_{\beta\gamma} + u_\beta \delta_{\gamma\alpha} + u_\gamma \delta_{\alpha\beta}$, and $\delta_{\alpha\beta}$ is the Kronecker delta function. $\Pi_{\alpha\beta\gamma}^{eq,theo}$ represents the third-order moment of the equilibrium function expected to recover exactly the Navier-Stokes equations. The discrete nature of the D3Q27 lattice is responsible for this moment not being properly fulfilled. In particular, one gets for $\Pi_{\alpha\beta\gamma}^{eq} = \sum_i e_{i\alpha} e_{i\beta} e_{i\gamma} f_i^{eq}$ that

$$\Pi_{\alpha\alpha\alpha}^{eq} = 3\rho c_s^2 u_\alpha, \tag{15}$$

$$\Pi_{\alpha\beta\gamma}^{eq} = \rho u_\alpha^2 u_\gamma + \rho c_s^2 u_\gamma \quad \text{if} \quad \alpha = \beta \neq \gamma \tag{16}$$

leading to the lattice isotropic defect

$$D_{\alpha\beta\gamma}^{eq} = \int e_\alpha e_\beta e_\gamma f_i^{eq} d\boldsymbol{e} - \Pi_{\alpha\beta\gamma}^{eq} = \Pi_{\alpha\beta\gamma}^{eq,theo} - \Pi_{\alpha\beta\gamma}^{eq} \neq 0 \tag{17}$$

The correction term $\mathrm{Corr}_{\alpha\beta}$ addresses explicitly this discrepancy (details are provided in Appendix B), which yields

$$\begin{aligned}\mathrm{Corr}_{\alpha\beta} = \quad & \delta_{\alpha\beta}\partial_t(p-\rho c_s^2) \\ & - u_\alpha\partial_\beta(p-\rho c_s^2) - u_\beta\partial_\alpha(p-\rho c_s^2) \\ & - \partial_\gamma D^{eq}_{\alpha\beta\gamma} \\ & + \delta_{\alpha\beta}\frac{2}{3}\rho c_s^2\partial_\gamma u_\gamma.\end{aligned} \tag{18}$$

This expression corresponds to Eq. (52) and Eq. (54) in reference[59] under the assumption of an ideal gas law $p = \rho\theta c_s^2$ and with $\kappa = 0$. In Eq. (18), the corrections terms will be discretized using finite difference schemes, employing a first-order backward scheme for the temporal derivative, a second-order central scheme for the divergence operator, and a first-order upwind scheme for the remaining spatial derivatives.

The classical BGK collision operator given by Eq. (3) suffers from numerical instability, particularly in high Reynolds flows. Consequently, various alternative collision operators have been proposed in the literature[68,69]. Following again Farag et al.[59], we adopt the third-order recursive regularized collision operator[70]. This means that instead of using Eq. (5), the non-equilibrium distribution functions are reconstructed from

$$\bar{f}_i^{neq} = w_i\left[\frac{H_{i\alpha\beta}\ a^1_{\alpha\beta}}{2c_s^4} + \frac{H_{i\alpha\beta\gamma}\ a^1_{\alpha\beta\gamma}}{6c_s^6}\right], \tag{19}$$

$$\text{with } a^1_{\alpha\beta} = \sum_i e_{i\alpha}e_{i\beta}f_i^{neq} \quad \text{and } a^1_{\alpha\beta\gamma} = \left[u_\alpha a^1_{\beta\gamma} + u_\beta a^1_{\alpha\gamma} + u_\gamma a^1_{\alpha\beta}\right]. \tag{20}$$

We recall that the second-order non-equilibrium moment in Eq. (20) is related to the stress tensor via the Chapmann-Enskog expansion, as

$$a^1_{\alpha\beta} = \tau\rho c_s^2\left[\partial^{(1)}_\alpha u_\beta + \partial^{(1)}_\beta u_\alpha - \delta_{\alpha\beta}\frac{2}{3}\partial^{(1)}_\gamma u_\gamma\right] + O(\epsilon^2). \tag{21}$$

To mitigate spurious pressure terms that may arise from the combination of numerical schemes (finite difference schemes in $\mathrm{Corr}_{\alpha\beta}$ and LB scheme) during the calculation of $a^1_{\alpha\beta}$ using Eq. (5) and Eq. (20), we enforce its trace to be zero by redistributing the potential discretization error as follows[59]:

$$\bar{a}^1_{\alpha\alpha} = a^1_{\alpha\alpha} - \frac{1}{3}a^1_{\beta\beta}. \tag{22}$$

Finally, in the collision step Eq. (3), the last term $F_i^{\mu_b}$ introduces an had-hoc artificial bulk viscosity to enhance stability at high Mach numbers:

$$F_i^{\mu_b} = -0.07\mathrm{Ma}^2\frac{w_i}{2c_s^4}H_{i\alpha\alpha}\rho c_s^2\partial_\alpha u_\alpha. \tag{23}$$

With the exception of leaving the pressure equation undefined and employing the D3Q27 velocity set, the present LB scheme is similar to the one proposed by Farag et al.[59]. This previous study opted for the entropy formulation for energy discretization due to its inherent property of decoupled linear stability. We adopt the strategy proposed more recently by Wissocq et al.[60] including a total energy formulation. This conservative form of the energy scheme ensures the recovery of the correct shock speed.

B. Finite-volume scheme for total energy

By adapting Riemann solvers to the LB formalism, Wissocq et al.[60] introduced a conservative scheme that is linearly equivalent to its non-conservative entropy formulation. In

particular, this scheme preserves the low dissipation characteristic of the LBM for isentropic phenomena such as acoustic propagation and vorticity. The conservative formulation for the total energy is expressed as

$$\partial_t \left(\rho E\right) + \partial_\alpha \mathcal{F}_\alpha^{\rho E} = 0, \tag{24}$$

where $\mathcal{F}_\alpha^{\rho E}$ denotes the total energy flux, encompassing both advective and diffusive components. Detailed expressions of these fluxes are provided in the study by Wissocq et al.[60]. These expressions depend not only on the macroscopic quantities (ρ, u_α, E) and the flux discretization scheme used, but also on the distribution functions f_i. Additional terms in $\mathcal{F}_\alpha^{\rho E}$ ensure consistency between the mass and momentum, solved by LBM, and the total energy solved by the finite-volume method. The same computational grid as the LBM is used. We tested four discretization schemes for the fluxes: a first-order upwind scheme, two MUSCL-Hancock schemes as suggested in references[59,60] (MHM1D) or in references[61,71] (MHM2D) and a TVD Heun scheme as used in Wissocq et al.[61].

C. Thermal and caloric equations of states

The governing equations require a model to establish the relationships between the thermodynamic variables p, ρ, and e. We need to provide the thermal and caloric EOS, respectively:

$$p = p\left(\rho, T\right) \quad \text{and } e = \left(\rho, T\right). \tag{25}$$

T denotes temperature, and e represents the density of internal energy (per unit mass), which is related to total energy through $E = e + \frac{1}{2} u_\alpha u_\alpha$. Both thermal and caloric EOS are linked via the relation

$$e = e_{ref} + \int_{T_{ref}}^{T} c_{v_\infty}\left(T'\right) dT' + \int_{\rho_{ref}}^{\rho} \left[T \left(\frac{\partial p}{\partial T} \right)_\rho - p \right] \frac{d\rho'}{\rho'^2}, \tag{26}$$

where the $_{ref}$ subscript refers to an arbitrary reference state, c_{v_∞} denotes the specific heat at constant volume in the ideal gas limit. The last term in Eq. (26) represents the deviation from the assumption of calorically perfect gas and is contingent upon the EOS. Following Guardone and Argrow[72], the ideal isochoric heat capacity can be approximated by a power law of the form

$$c_{v_\infty}(T) = c_{v_\infty}(T_c) \left(\frac{T}{T_c} \right)^n, \tag{27}$$

with T_c denoting the critical temperature, and $c_{v_\infty}(T_c)$ and n being dependent on the simulated gas.

In this study, we consider three thermal equations. The simplest relation, known as the ideal gas assumption, is valid in the dilute gas region:

$$p(\rho, T) = \rho R_g T, \tag{28}$$

where R_g denotes the specific gas constant. The van der Waals EOS refines the ideal gas assumption by considering the finite size of gas molecules and the attractive forces between them:

$$p(\rho, T) = \frac{\rho R_g T}{1 - b\rho} - a\rho^2, \tag{29}$$

where the a and b parameters depends on the critical pressure p_c and temperature T_c as follows:

$$a = \frac{27 R_g^2 T_c^2}{64 p_c} \quad \text{and } b = \frac{R_g T_c}{8 p_c}. \tag{30}$$

More complex yet more accurate EOS are necessary to realistically explore the non-classical gas dynamic phenomena. Third-order thermal EOS have been found to offer a good compromise in terms of complexity and accuracy. They have been validated in the thermodynamic region where non-classical gas phenomena are expected to be observed for heavier substances[73]. One the available third-order EOS is the Peng-Robinson EOS[48]. It is expressed as

$$p(\rho, T) = \frac{\rho R_g T}{1 - b\rho} - \frac{a(T)\rho^2}{1 + 2b\rho - b^2\rho^2}, \tag{31}$$

where

$$a = 0.45724 \frac{R_g^2 T_c^2}{p_c} \alpha(T) \quad \text{and } b = 0.07780 \frac{R T_c}{p_c}, \quad \text{with } \alpha(T) = \left(1 + \kappa(\omega)(1 - \sqrt{T/T_c})\right)^2, \tag{32}$$

where a relates to the attractive effect of van der Waals forces and b to the effective molar volume. The κ coefficient varies according to the accentric factor ω, which measures the non-sphericity of molecules of the selected gas.

$$\kappa(\omega) = 0.37464 + 1.54226\omega - 0.26992\omega^2, \quad \text{if } \omega \leq 0.491 \tag{33}$$

$$\kappa(\omega) = 0.379642 + 1.487503\omega - 0.164423\omega^2 + 0.016666\omega^3, \quad \text{if } \omega > 0.491 \tag{34}$$

Obtaining the temperature as a function of internal energy and density from Eq. (26) for the Peng-Robinson EOS is not straightforward. We resort to an iterative Newton-Raphson method to compute $T = T(\rho, e)$.

Finally, the gas viscosity and thermal conductivity must be described according to the thermodynamic variables. When the perfect gas assumption is involved, the Sutherland law for air and a constant Prandtl number equal to 0.71 is used. For dense gas simulations, we use the generalized laws for viscosity and thermal conductivity developed by Chung et al.[49].

D. Summary of the hybrid compressible lattice Boltzmann algorithm for non-ideal gases

The hybrid compressible lattice Boltzmann algorithm for non-ideal gases is depicted in the flowchart presented in Figure 2.

Finally, we would like to highlight that this algorithm has been ported to a multi-GPU architecture, offering advantageous execution times. For instance, the perfect and dense gas TGV simulations presented later, at a resolution of $N = 768$ with the MHM2D flux-reconstruction scheme, were completed in approximately 2.25 and 6 hours, respectively, using two AMD MI250x cards in double precision.

III. VALIDATION

In this section, the hybrid lattice Boltzmann method for non-ideal fluids is validated across two distinct scenarios. Firstly, we showcase its capability to capture the non-classical behavior of a BZT gas within a shock tube. Secondly, we assess its effectiveness in simulating compressible turbulence by considering the Taylor-Green vortex flow. Each case demonstrates its correctness and accuracy in capturing complex fluid dynamics.

A. Non-classical van der Waals shock tube

Shock tube simulations are a standard one-dimensional test problem for evaluating numerical schemes. In the context of BZT fluids, they offer the opportunity to showcase a

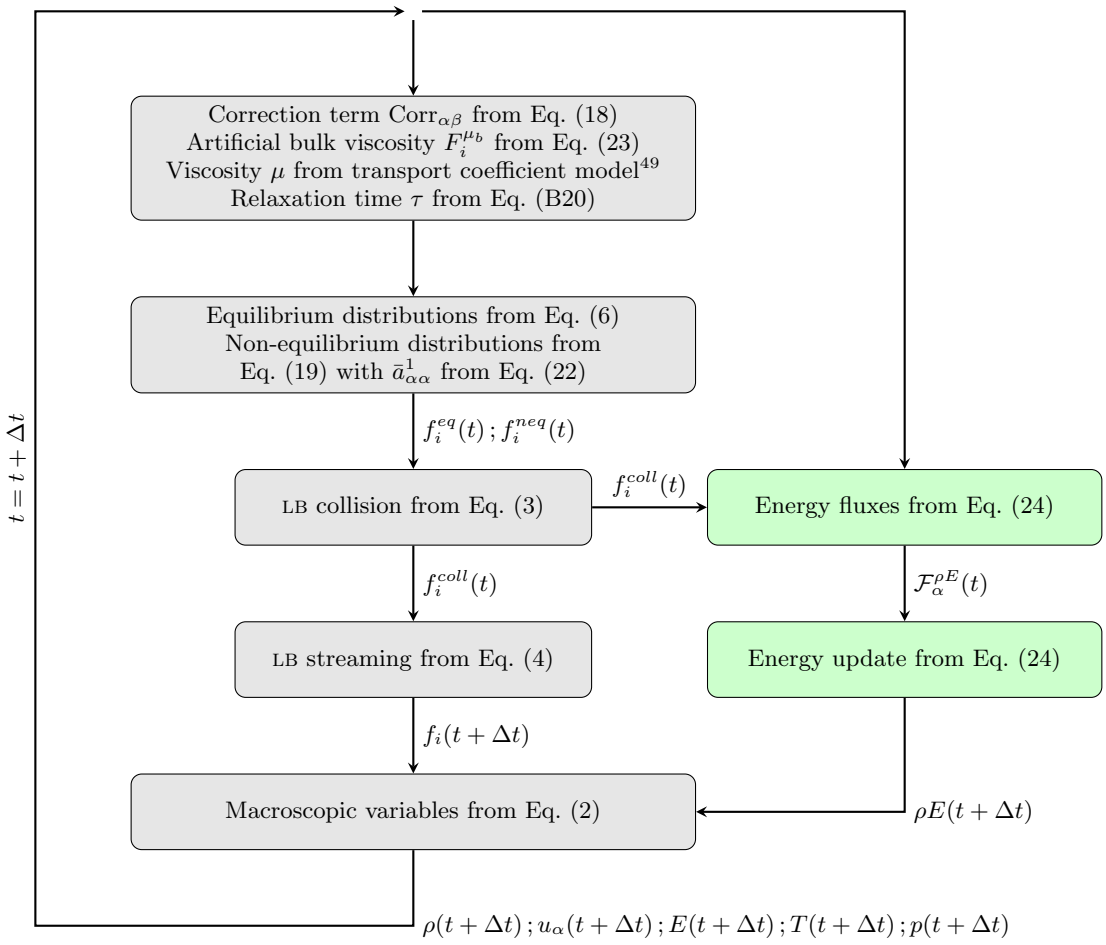

FIG. 2: Temporal flowchart of the proposed algorithm, with spatial dependencies between steps omitted for clarity.

non-classical shock behavior. The fluid is assumed to be calorically perfect and modeled by the van der Waals EOS, with the thermodynamic properties summarized in Table I. Viscosity is set to zero. A 1000-point grid represents a one-meter length tube, $L = 1\mathrm{m}$. Additionally, we define a dimensionless time as $t^* = t/L \times \sqrt{p_c/\rho_c}$ and choose a constant time step of $\Delta t^* = 9 \times 10^{-4}$ resulting in a Courant–Friedrichs–Lewy number close to 0.92. The first-order upwind scheme is used for the energy fluxes. Table II lists the selected initial state on both sides of the diaphragm. Both states are located in the BZT region where $\Gamma < 0$.

$\mathcal{M}$ [kg.mol^{-1}]	T_c [K]	p_c [atm]	$c_{v_\infty}(T_c)/R_g$ [−]
0.574	632.15	15.98	1/0.0125

TABLE I: Thermodynamic properties of the gas used in the shock tube case. Van der Waals EOS is considered.

The reduced density and pressure and the fundamental derivative of gas are shown at different times in Fig. 3. This case is representative of the non-classical behavior of a BZT fluid, where an expansion shock moves to the left and a compression fan moves to the right, with a contact discontinuity connecting both waves. The results are in close agreement with the simulation of Guardone and Vigevano, who used a Roe linearization method for

	p/p_c	ρ/ρ_c
left	1.090	0.879
right	0.885	0.562

TABLE II: Initial conditions for the shock tube case, "D2" case in Argrow[74] or "DG2" case in Guardone and Vigevano[75].

the van der Waals gas[75], as well as with the results obtained by Reyhanian et al.[63] with an *off-lattice* LB scheme. However, in contrast to this latter simulation, no overshoot at the expansion shock is visible in our case. The current simulation confirms the capacity of the hybrid LBM to accurately capture the non-classical behavior of gases in the BZT region.

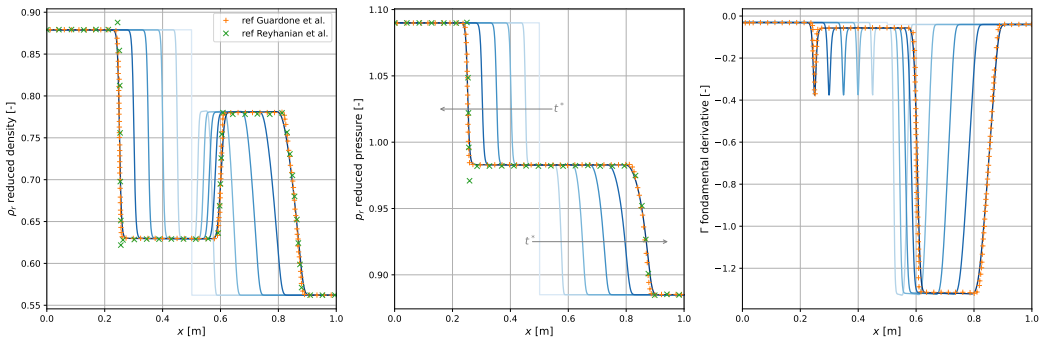

FIG. 3: Numerical solution of the shock tube problem. Solution at the dimensionless time $t^* = 0, 0.09, 0.18, 0.27, 0.36, 0.45$. Lines with color gradient indicating the time evolution: present simulation, markers at $t^* = 0.45$; Orange marker + from Guardone and Vigevano[75] and green marker x from Reyhanian et al.[63]. Close agreement is obtained.

The shock tube test case has served as a valuable benchmark for evaluating the ability of our scheme to handle steep gradients, or discontinuities, without introducing numerical artifacts such as spurious oscillations (dispersion errors), which is an essential prerequisite for compressible flow simulations. The Taylor-Green vortex flow test case is now considered by introducing turbulence associated with the complex entanglement of compressible vortex structures. Together, these two test cases are expected to provide a more comprehensive assessment of the robustness and accuracy of our scheme in handling a wide range of compressible flow situations.

B. Compressible Taylor-Green vortex flow with a perfect gas

The Taylor-Green Vortex (TGV) flow is a standard test case that exhibits a transition from laminar to turbulent flow in a decaying regime. This flow is a popular benchmark to evaluate the accuracy and efficiency of numerical schemes. However, it is usually examined under the condition of incompressibility or at low Mach number ($\mathrm{Ma} \lesssim 0.1$). The effect of compressibility on the TGV flow has only recently been examined. In that situation, the interaction of multiple shock waves makes this configuration particularly challenging. Peng and Yang[76] described the evolution of the vortex-surface fields in (perfect gas) compressible TGV flows at Reynolds number $\mathrm{Re}_0 = 800$ and Mach number up to $\mathrm{Ma}_0 = 2$. Lusher and Sandham[77] compared different shock-capturing schemes up to Mach number $\mathrm{Ma}_0 = 1.25$ at $\mathrm{Re}_0 = 1600$. Wilde et al.[78] simulated this later case to validate a semi-Lagrangian lattice Boltzmann method combining *off-lattice* and *multispeed* strategies. Similarly, we validate our approach with the perfect gas compressible TGV flow and extend this flow configuration to dense gas.

The fluid domain of the TGV flow is a three-dimensional periodic box of size $0 \leq x, y, z \leq 2\pi L$. The initial solution includes counter-rotating vortices and is given by

$$u_x(x, y, z, t = 0) = U_0 \sin(\frac{x}{L}) \cos(\frac{y}{L}) \cos(\frac{z}{L}), \tag{35}$$

$$u_y(x, y, z, t = 0) = -U_0 \cos(\frac{x}{L}) \sin(\frac{y}{L}) \cos(\frac{z}{L}), \tag{36}$$

$$u_z(x, y, z, t = 0) = 0, \tag{37}$$

$$p(x, y, z, t = 0) = p_0 + \frac{\rho_0 U_0^2}{16} \left[\cos(\frac{2x}{L}) + \cos(\frac{2y}{L})\right] \left[\cos(\frac{2z}{L}) + 2\right], \tag{38}$$

$$T(x, y, z, t = 0) = T_0, \tag{39}$$

The initial density field is obtained from the thermal EOS.

In the ideal gas configuration, the operating point is located within the dilute region with $T_0 = 293.15$, $\rho_0 = 1.204$, $R_g = 287.05$, $p_0 = \rho_0 R_g T_0$, and a heat capacity ratio $\gamma = 1.4$. The reference velocity U_0 is determined by the initial Mach number, while the length L is defined by the initial Reynolds number. We set $\mathrm{Ma}_0 = U_0/c_0 = 1$, resulting in an initial turbulent Mach number of 0.5, and $\mathrm{Re}_0 = L\rho_0 U_0/\mu_0 = 1600$ for all TGV simulations presented in this article. Simulations are advanced until a non-dimensional time of $t^* = t/t_{conv} = 20$, where the convective time is defined as $t_{conv} = L/U_0$. A fixed time step is set for all simulations, given by $\Delta t^* = 0.012 \times 128/N$, where N denotes the grid resolution. This yields an initial Courant–Friedrichs–Lewy number of 0.49 for all grids.

Fig. 4 addresses the grid resolution sensitivity for $N = 128, 256, 384, 512$ and 768 with the MUSCL-Hancock scheme based on the total energy (MHM2D[61,71]). We plot the dimensionless mean kinetic energy, E_k, and enstrophy or solenoidal viscous dissipation, E_n, defined respectively as

$$E_k = \langle \frac{1}{2} \rho u_i u_i \rangle \frac{1}{\rho_0 U_0^2}, \tag{40}$$

$$E_n = \langle \frac{1}{2} \mu |\boldsymbol{\omega}|^2 \rangle \frac{L}{\rho_0 U_0^3}, \tag{41}$$

where $\langle \cdot \rangle$ indicates averaging over the whole grid, and $\boldsymbol{\omega} = \nabla \times \mathbf{u}$ represents the vorticity of the fluid and μ its dynamic viscosity. Our results are compared with those of Lusher and Sandham[77], who applied a sixth-order targeted essentially non-oscillatory (TENO) scheme on a 512^3 grid.

The kinetic energy shows little sensitivity to changes in grid size, unlike the enstrophy. For $N = 128$ and 256, the enstrophy is significantly underestimated. A closer agreement is observed between $N = 384$, $N = 512$ and $N = 768$. As N increases, vanishing discrepancies are only observed near the plateau around $t^* = 9$, at the moment of the maximum enstrophy ($t^* \approx 11.2$), and during the decrease that follows immediately ($11.2 < t^* < 13$). The enstrophy perfectly matches the reference for $N = 768$. The maximum Mach number over the entire domain acts as a sharp indicator of grid convergence. At grid resolutions of $N = 512$ and $N = 768$, the differences are marginal, demonstrating that the simulations accurately capture discontinuities with minimal numerical dissipation. This consistency suggests that the $N = 768$ grid size is sufficient to effectively resolve the critical flow features.

Fig. 5 compares, at a fixed resolution $N = 512$, different flux-reconstruction schemes used in the finite-volume integration of the total energy equation. All schemes yield similar results. The upwind scheme better captures the enstrophy plateau, whereas the MUSCL-Hancock methods (MHM1D and MHM2D) are less dissipative near the maximum of enstrophy. The MHM2D scheme offers the best accuracy, however, the improvement over the MHM1D scheme is only marginal in this test case.

Following the grid-sensitivity analysis and flux-reconstruction-scheme comparisons, the next TGV flow simulations will be performed by using the MHM2D scheme with a $N = 768$ grid size.

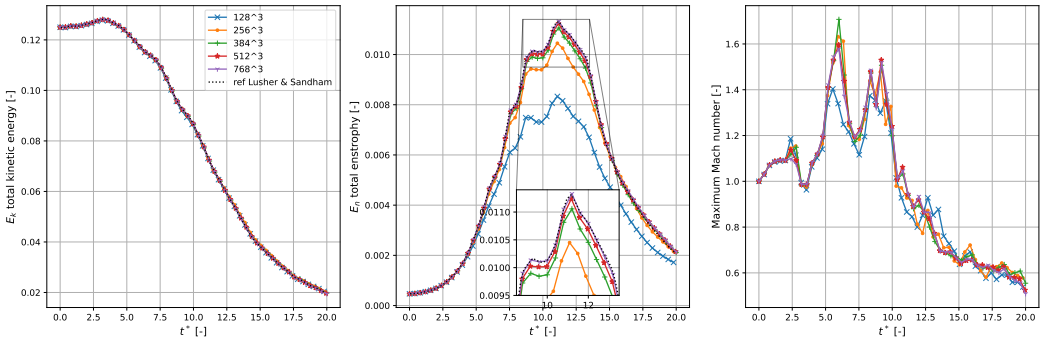

FIG. 4: Influence of the grid resolution on the mean kinetic energy (left) and enstrophy (middle), and the maximum Mach number (right) for the perfect gas compressible TGV flow at $\mathrm{Ma}_0 = 1$, using the MHM2D scheme for the total energy. The dotted black lines of Lusher and Sandham[77] are perfectly superimposed on the plots of the $N = 512$ and $N = 768$ simulations for the energy and enstrophy, demonstrating grid convergence.

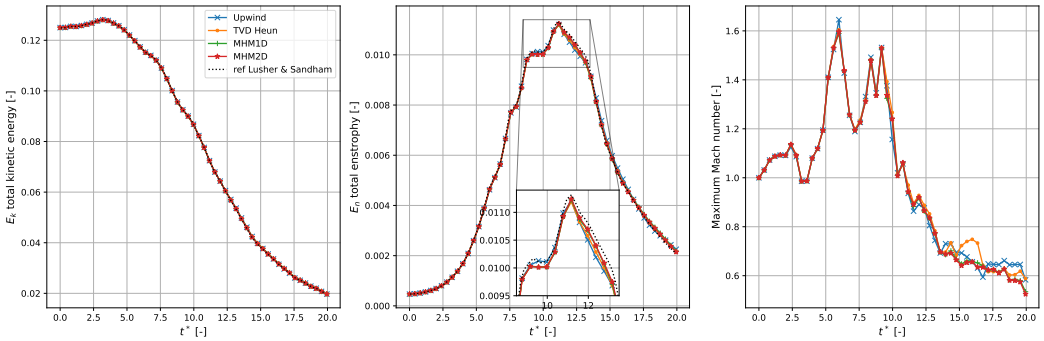

FIG. 5: Influence of the finite-volume scheme on the mean kinetic energy (left) and enstrophy (middle), and the maximum Mach number (right) for the perfect gas compressible TGV flow at resolution $N = 512$. Dotted black line from Lusher and Sandham[77]. Marginal improvements are observed according to the finite-volume schemes used for the total energy.

IV. TAYLOR-GREEN VORTEX FLOW WITH A DENSE GAS

Sciacovelli et al.[79] were the first to investigate the impact of dense gas effects on decaying compressible homogeneous isotropic turbulence. They employed the van der Walls thermal EOS, assuming a calorically perfect gas, and neglected viscous effects. Later, the same authors[22] focused on viscous effects occurring in the small-scale dynamics of dense gas decaying compressible homogeneous isotropic turbulence. They used the Martin-Hou EOS and the Chung formulation for transport coefficients to represent the dense gas behavior more accurately. Subsequently, Giauque et al.[80] continued the study by considering isotropic homogeneous forced turbulence to extend the time span and analyze turbulence in a quasi-stationary context. In this section, the impact of dense gas effects on the transition from laminar to turbulent flow in a decaying vortex is investigated. The well-known Taylor-Green vortex (TGV) flow has never been studied in the context of a BZT gas. We consider the dense gas named perfluorotripentylamine (FC-70, $C_{15}F_{33}N$), modeled by the Peng-Robinson equation of state and the Chung formula for transport coefficients. The thermodynamic properties of the dense gas are provided in Table III.

The operating point for the dense gas simulation is taken within the inversion region, i.e.

$\mathcal{M}$ [kg.mol^{-1}]	T_c [K]	p_c [atm]	$c_{v_\infty}(T_c)/R_g$ [−]	Z_c [−]	n [−]	ω [−]
0.821	608.2	10.2	118.7	0.270	0.4930	0.7584

TABLE III: Thermodynamic properties of the dense gas FC-70. Peng-Robinson EOS is used.

$\Gamma < 0$, with initial conditions $p_0 = 0.96p_c$ and $\rho_0 = \rho_c/1.65$ resulting in a compressibility factor $Z_0 = p_0/(\rho_0 R_g T_0) \approx 0.43[-]$ as indicated in Fig. 6. Contrary to section III B in Eq (38), the initial pressure field is constant $p(x, y, z, t = 0) = p_0$. It was observed that this modification, which allows the system to adapt the pressure field to the velocity field by itself, was necessary to avoid crossing the saturation line and the presence of a liquid phase during the simulation. The perfect gas simulation follows a similar setup and operating point to the previous section III B, but with an initial constant pressure field. Fig. 7 shows the influence of the grid resolution on the total kinetic energy, enstrophy and maximum Mach number for the dense gas simulation. The minor differences between $N = 512$ and $N = 768$ indicate that a grid size of $N = 768$ allows for an accurate resolution of all scales of motion, much like the perfect gas simulation with a non-constant initial pressure field.

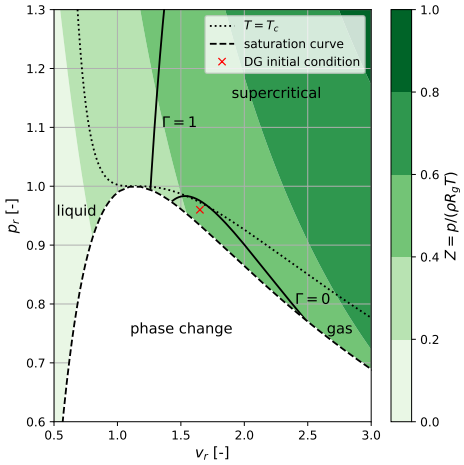

FIG. 6: $p_r - v_r$ diagram of the FC-70 gas with the Peng-Robinson EOS. The red cross marks the initial condition for the dense gas simulation.

The TGV flows for perfect and dense gases at an initial Mach number of one are now compared. Fig. 8 displays the temporal evolution of the dimensionless kinetic energy and dimensionless enstrophy (solenoidal viscous dissipation) integrated over the entire domain and the evolution of the maximum local Mach number.The initial drop in kinetic energy during the first convective (or acoustic) time ($0 < t^* < 2$) indicates a transfer from kinetic to internal energy, attributed to the "imbalanced" (constant) initial pressure field. Conversely, the kinetic energy increases during the early stage ($2 < t^* < 4$) of the flow, consistent with the simulation with a non-constant initial pressure field as well as with previous observations[76,77]. Two small peaks appear later, indicating subsequent internal to kinetic energy conversions. The evolution of kinetic energy and enstrophy in both perfect and dense gas simulations follow a similar trend, except for an enstrophy plateau in the perfect gas case compared to a peak in the dense case. In contrast to the previous plots, the evolution of the maximum Mach number differs significantly between the perfect and dense gas simulations until the enstrophy reaches its maximum value, i.e. approximately $t^* \approx 9$.

In Fig. 9, the (isotropic) kinetic energy spectra $\|\widehat{\sqrt{\rho}u'_\alpha}\|^2(k)$ normalized by $\rho_0 U_0^2$ are plotted as a function of the wavenumber $k = \|\boldsymbol{k}\|$ at different times for the perfect gas

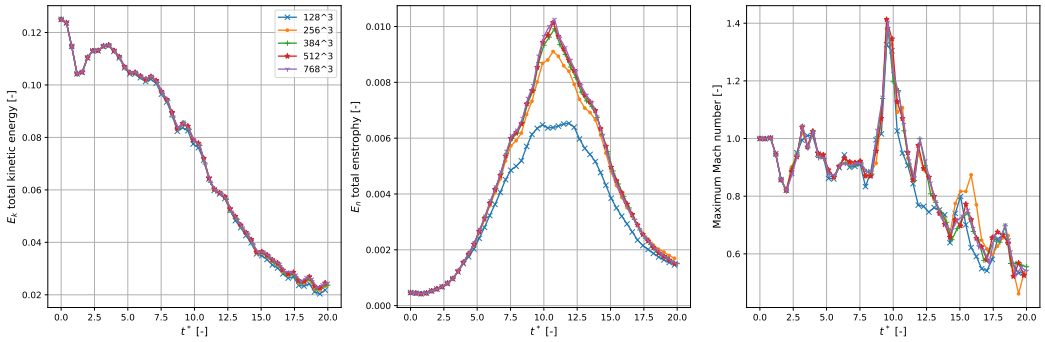

FIG. 7: Influence of the grid resolution on the total kinetic energy, total enstrophy, and maximum Mach number for the dense gas compressible TGV flow at $\mathrm{Ma}_0 = 1$. The minor differences between $N = 512$ and $N = 768$ indicate that a grid size of $N = 768$ allows for an accurate resolution of all scales of motion.

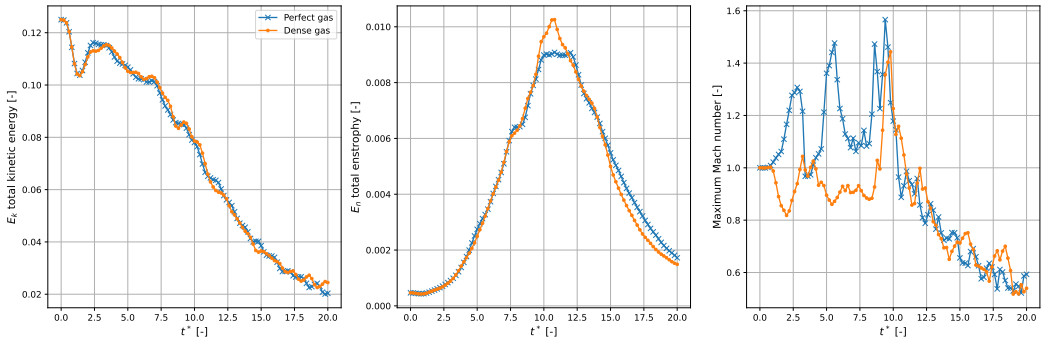

FIG. 8: Total kinetic energy, total enstrophy and maximum Mach number for perfect gas and dense gas compressible TGV flow at $\mathrm{Ma}_0 = 1$. A similar trend is observed in integrated quantities like total energy and total enstrophy; however, local values, such as the maximum Mach number, differ significantly.

and dense gas TGV simulations, both initialized with a constant pressure field. Given the definition of the TGV flow, the spectra are initially fed at $k = 2k_0 = 4\pi/L$. An intense energy transfer then operates from low to high wavenumbers driven by the quadratic nonlinearity of gas dynamics. For the perfect gas simulation, more energy is contained in the (very) small scales ($k^* > 50$) compared to the dense gas simulation up to $t^* < 6$. For $t^* > 6$, the turbulent kinetic energy spectra become similar for the perfect and dense gas cases and exhibit a classical $k^{-5/3}$ Kolmogorov power-law scaling. To examine the influence of the initial pressure field, a simulation initialized with a non-constant pressure (cf III B) is also considered for the perfect gas. The growth of the small-scale structures is slower in this case. However, by $t^* = 6$, the kinetic energy spectrum reaches and maintains a similar level to that observed with a constant initial pressure field. This suggests that the initial pressure field has a minor influence (after a short transient period) on the subsequent distribution of kinetic energy across the different scales of motion.

So far, the differences between TGV simulations of perfect and dense gas have been relatively small. However, as the shock tube results reported in section III A indicate, a distinct feature of dense gases is related to fluid expansions and compressions. In Fig. 10, we plot the dilatation field $\theta(\boldsymbol{x}, t) = \partial_\alpha u_\alpha(\boldsymbol{x}, t)$ normalized by its standard deviation at time $t^* = 9.5$ in a slice at $x = L/5$ for both gases. At this instant, the maximum Mach number (in the whole domain) is high, above 1.4. Four symmetric quadrants reminiscent of the initial condition are visible in the slice for both gases, but the dilatation field shows distinct differences

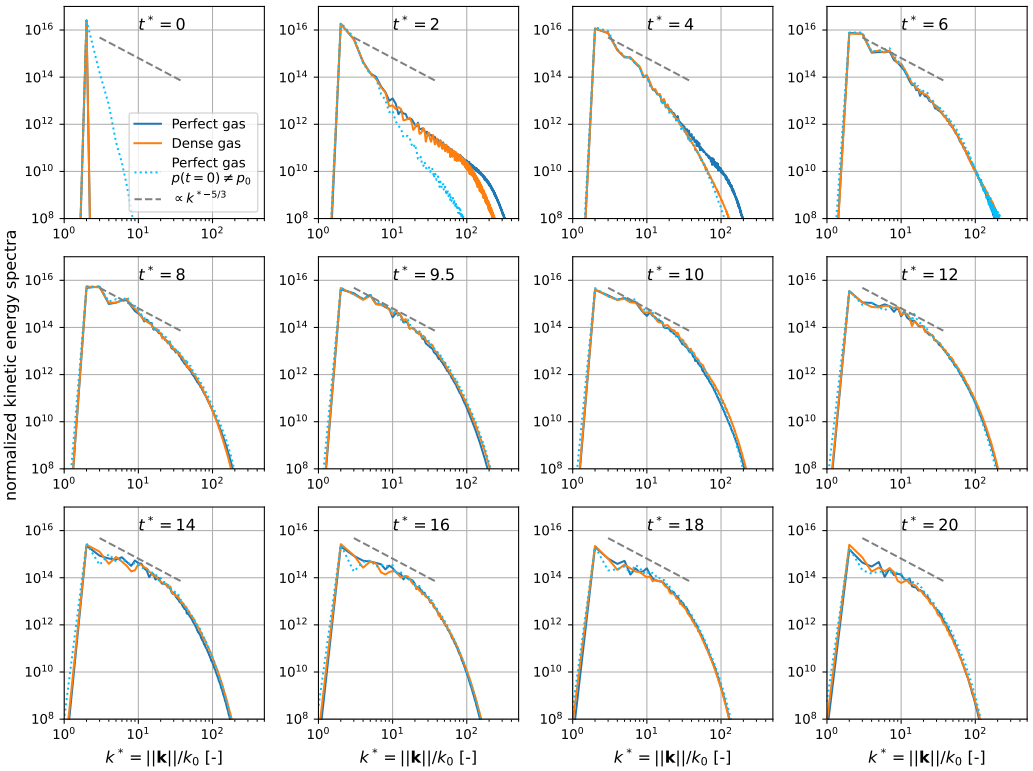

FIG. 9: Turbulent kinetic energy spectra at different times for the compressible TGV flow; $k_0 = \frac{2\pi}{L}$. The light blue dotted line corresponds to a perfect gas with an initial non-constant pressure field given by Eq. (38). The blue and orange continuous lines refer to simulations with an initial constant pressure field $p(\boldsymbol{x}, 0) = p_0$ for the perfect and dense gas, respectively. At early times, the perfect gas simulation contains more kinetic energy in the small scales than the dense gas simulation.

between the perfect and dense gas. In particular, thin layers of moderate compression are visible in the perfect gas but not in the dense gas. The supersonic flow, contained in the area delimited by the green isocontour $\mathrm{Ma} = 1$, occurs in small regions at the same locations for both gases. However, as already observed in homogeneous isotropic turbulence[79,80], large expansions (red spots where $\theta/\theta_{\mathrm{std}} > 5$) are only present in the dense gas simulation, inside these supersonic regions.

Previous results suggest that integral quantities behave similarly for perfect and dense gas in the compressible TGV flow at initial $\mathrm{Ma}_0 = 1$. Nevertheless, the maximum Mach number along the simulation differs between the two gases as the flow decays, as shown in Fig. 8. To highlight how spatial fluctuations evolve during the simulation, we plot the standard deviation normalized by the averaged value over the entire domain at different times for the pressure, density, temperature, dynamic viscosity (μ), thermal conductivity (λ) and speed of sound (c)in Fig. 11. Mass densities show the same level of fluctuations. However, for the pressure and temperature variations, the level of fluctuations is up to five times lower in the dense gas than in the perfect gas. The almost isothermal behavior of the dense gas can be attributed to its larger heat capacity. This is also reflected in the Eckert number of the flow, defined as the ratio between kinetic energy and enthalpy, i.e. $\mathrm{E_c} = U_0^2/c_{p_0}T_0$. For the dense gas, the Eckert number at the initial operating point is significantly lower with $\mathrm{E_{cDG}} \approx 6\ 10^{-4}$ compared to $\mathrm{E_{cPG}} = 0.4$ for the perfect gas. On the other hand, viscosity and speed of sound exhibit greater spatial variation in the dense gas, primarily due to fluctuations in density (or pressure).

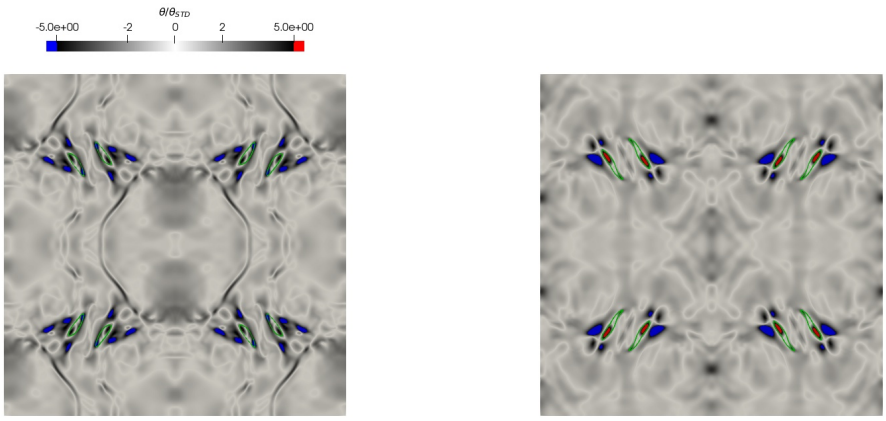

FIG. 10: Normalized dilatation field $\theta/\theta_{\text{std}}$ at time $t^* = 9.5$ in the slice $x = L/5$. The green curves represent the isocontours Ma = 1. The color map is saturated at ± 5 to highlight large compression and expansion events. Left: perfect gas; Right: dense gas. Large expansions occur only in the dense gas simulation, specifically within the supersonic regions.

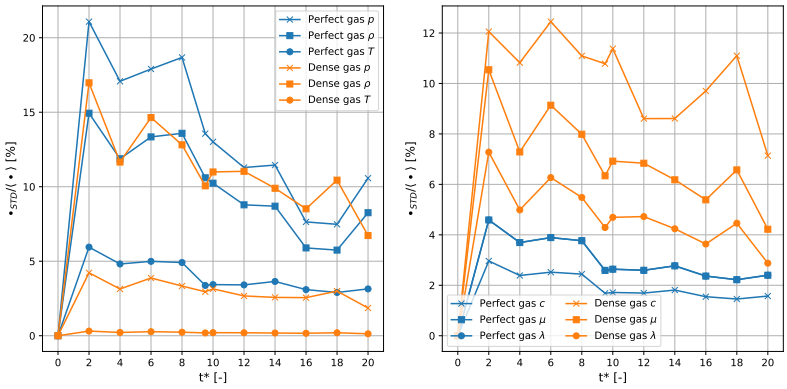

FIG. 11: Relative standard deviation (in space) along time for the perfect and dense gases. Left: state variables p, ρ, T; Right: transport coefficients μ (dynamic viscosity), λ (thermal conductivity) and speed of sound c. Because of the constant Prandtl assumption, μ and λ remain proportional in the perfect gas. The state variables, transports coefficients, and speed of sound evolve differently for the dense gas and perfect gas.

V. CONCLUSION AND PERSPECTIVES

To answer the needs of the energy transition, designing efficient ORC turbines require new numerical methods capable of handling complex flow structures (such as expansion shock-waves and compressible turbulence) arising from the non-ideal thermodynamic behavior of the fluids at play. This paper presents a novel hybrid lattice-compressible Boltzmann method suitable for simulating turbulent BZT dense gas flows. This method integrates a third-order Peng-Robinson EOS and Chung's transport coefficient model, thereby enhancing the capacity of the conventional LBM to manage non-ideal fluids. The proposed hybrid scheme addresses the challenges of simulating highly compressible flows by combining the strengths of the LBM and the finite-volume method for handling the evolution of the total energy. The validation was conducted through two distinct test cases: the non-classical behavior of a BZT gas within a shock tube and the compressible TGV flow. The results

from the shock tube simulations aligned closely with existing literature, validating the method's accuracy in capturing non-classical shock behaviors, such as rarefaction shock waves. For the TGV flow, an in-depth analysis of the sensitivity to the grid resolution and flux-reconstruction scheme (for the total energy) has been carried out, confirming the effectiveness of the method in simulating compressible turbulence. Simulations demonstrated the algorithm's ability to capture strong compressibility effects, using high grid resolution and advanced flux reconstruction schemes. A significant contribution of this work is the first application of hybrid LBM to investigate dense and BZT effects in a TGV flow configuration. The simulations revealed significant differences between dense and perfect gas flows at the same initial Mach number, underlining the importance of taking into account the effects of non-ideal gases in the analysis of compressible turbulence.

Future work includes the study and development of new numerical flow schemes to ensure numerical stability while maintaining accessible grid resolution, at even higher Mach numbers, more representative of industrial ORC applications. The treatment of boundary conditions is another important project in perspective. When simulating flows in ORC turbines, handling boundary conditions is particularly challenging due to the interaction of shock waves with solid structures. These interactions can lead to complex phenomena such as shock reflections, boundary layer separation, and pressure wave distortions, which require precise treatments to be properly captured. The lattice Boltzmann scheme, being constrained by its fixed Cartesian grid, further complicates the situation and requires the use of immersed boundary techniques to account for arbitrarily curved, possibly moving, solid boundaries. This requires careful interpolation and boundary force modeling to accurately represent the dynamics of fluid-structure interaction, especially in the presence of highly-compressible and high-speed flows typical of ORC turbines. To the best of our knowledge, this remains an open area of research, pushing the limits of current lattice Boltzmann-based simulation capabilities.

Finally, we would like to mention that, although our simulations do not reach the Mach regimes encountered in the targeted ORC turbine simulations, they nevertheless serve as a significant benchmark. They ensure that our hybrid LBM scheme can effectively address the complexities of compressible flows, such as capturing shock waves and handling high density and pressure gradients, which represent the basis of the phenomena observed at higher speeds. In this regard, we believe it represents a valuable step towards modeling real-world compressible flows encompassing non-ideal gas.

Appendix A: Hermite polynomials

The H_i's are discrete tensor Hermite polynomials in the velocity $\mathbf{e}$ and serve as a basis for the expansion of the discrete distribution functions. Zero, first, second, and third-order Hermite polynomials are

$$H_{i0} = 1, \tag{A1}$$
$$H_{i\alpha} = e_{i\alpha}, \tag{A2}$$
$$H_{i\alpha\beta} = e_{i\alpha}e_{i\beta} - c_s^2\delta_{\alpha\beta}, \tag{A3}$$
$$H_{i\alpha\beta\gamma} = e_{i\alpha}e_{i\beta}e_{i\gamma} - c_s^2(e_{i\alpha}\delta_{\beta\gamma} + e_{i\beta}\delta_{\alpha\gamma} + e_{i\gamma}\delta_{\alpha\beta}), \tag{A4}$$

with $0 \leq i < 26$ for the D3Q27 velocity set. Here, $\alpha, \beta, \gamma \in \{x, y, z\}$ and $c_s = 1/\sqrt{3}$.

Appendix B: Chapman-Enskog expansion

Macroscopic fluid dynamics follows from seeking solutions to the hierarchy of statistical equations that vary on a much slower timescale than the collisional timescale τ. This is usually done by using a multiple-timescales *Chapman-Enskog expansion* in the small

parameter ϵ, with

$$\begin{aligned} f_i &= f_i^{(0)} + \epsilon f_i^{(1)} + +\epsilon^2 f_i^{(2)} + \cdots \\ \partial_t &= \epsilon \partial_t^{(1)} + \epsilon^2 \partial_t^{(2)} + \cdots \\ \partial_\alpha &= \epsilon \partial_\alpha^{(1)} \end{aligned} \tag{B1}$$

The parameter ϵ may be identified physically with the Knudsen number.
The Taylor expansion up to the second order of $f_i(t + \Delta t, \boldsymbol{x} + \boldsymbol{e_i}\Delta t)$ gives

$$f_i(t + \Delta t, \boldsymbol{x} + \boldsymbol{e_i}\Delta t) - f_i(t, \boldsymbol{x}) = \Delta t(\partial_t + e_{i\alpha}\partial_\alpha) f_i + \frac{(\Delta t)^2}{2}(\partial_t + e_{i\alpha}\partial_\alpha)^2 f_i \tag{B2}$$

$$\Delta t(\partial_t + e_{i\alpha}\partial_\alpha) f_i + \frac{(\Delta t)^2}{2}(\partial_t + e_{i\alpha}\partial_\alpha)^2 f_i = -\frac{\Delta t}{\tau}(f_i - f_i^{eq}) + \Delta t(1 - \frac{\Delta t}{2\tau}) S_i \tag{B3}$$

At different orders, one obtains

$$O(\epsilon^0): \quad f_i^{(0)} = f_i^{eq} \tag{B4}$$

$$O(\epsilon^1): \quad \left(\partial_t^{(1)} + e_{i\alpha}\partial_\alpha^{(1)}\right) f_i^{(0)} = -\frac{1}{\tau} f_i^{(1)} + (1 - \frac{\Delta t}{2\tau}) S_i \tag{B5}$$

$$O(\epsilon^2): \quad \partial_t^{(2)} f_\alpha^{(0)} + \left(\partial_t^{(1)} + e_{i\alpha}\partial_\alpha^{(1)}\right) f_i^{(1)} + \frac{\Delta t}{2}\left(\partial_t^{(1)} + e_{i\alpha}\partial_\alpha^{(1)}\right)^2 f_\alpha^{(0)} = -\frac{1}{\tau} f_i^{(2)} \tag{B6}$$

Simplifying the second-order equation using the first-order yields

$$O(\epsilon^2): \quad \partial_t^{(2)} f_\alpha^{(0)} + \left(\partial_t^{(1)} + e_{i\alpha}\partial_\alpha^{(1)}\right)(1 - \frac{\Delta t}{2\tau})(f_i^{(1)} + \frac{\Delta t}{2} S_i^{(1)}) = -\frac{1}{\tau} f_i^{(2)} \tag{B7}$$

Taking the zeroth, first, and second moments of Eq. (B5) yields

$$\partial_t^{(1)} \rho + \partial_\alpha^{(1)}(\rho u_\alpha) = 0, \tag{B8}$$

$$\partial_t^{(1)}(\rho u_\alpha) + \partial_\beta^{(1)} \Pi_{\alpha\beta}^{eq} = 0, \tag{B9}$$

$$\partial_t^{(1)} \Pi_{\alpha\beta}^{eq} + \partial_\gamma^{(1)} \Pi_{\alpha\beta\gamma}^{eq} = -\frac{1}{\tau} \Pi_{\alpha\beta}^{(1)} + (1 - \frac{\Delta t}{2\tau}) \mathrm{Corr}_{\alpha\beta}^{(1)} \tag{B10}$$

Similarly, computing the zeroth, first, and second moments of Eq. (B7) gives

$$\partial_t^{(2)} \rho = 0 \tag{B11}$$

$$\partial_t^{(2)}(\rho u_\alpha) + \partial_\beta^{(1)}\{(1 - \frac{\Delta t}{2\tau})[\Pi_{\alpha\beta}^{(1)} + \frac{\Delta t}{2} \mathrm{Corr}_{\alpha\beta}^{(1)}]\} = 0. \tag{B12}$$

$\Pi_{\alpha\beta}^{(1)}$ is still unknown but can be expressed using Eq. (B10) at order $O(\epsilon)$. Recalling that $\partial_\alpha(abc) = a\partial_\alpha(bc) + b\partial_\alpha(ac) - ab\partial_\alpha(c)$ and using Eqs. (13, B8, B9), one gets

$$\partial_t^{(1)} \Pi_{\alpha\beta}^{eq} = -\partial_\gamma^{(1)}(\rho u_\alpha u_\beta u_\gamma) - (u_\alpha \partial_\beta^{(1)} p + u_\beta \partial_\alpha^{(1)} p) + \delta_{\alpha\beta} \partial_t^{(1)} p, \tag{B13}$$

and with the definition Eq. (14) and Eq. (B8), one obtains

$$\partial_\gamma^{(1)} \Pi_{\alpha\beta\gamma}^{eq} = \partial_\gamma^{(1)}(\Pi_{\alpha\beta\gamma}^{eq,theo} - D_{\alpha\beta\gamma}^{eq}) \tag{B14}$$

$$= \partial_\gamma^{(1)}(\rho u_\alpha u_\beta u_\gamma) - \partial_\gamma^{(1)} D_{\alpha\beta\gamma}^{eq} + c_s^2 \partial_\beta^{(1)}(\rho u_\alpha) + c_s^2 \partial_\alpha^{(1)}(\rho u_\beta) + \delta_{\alpha\beta} c_s^2 \partial_\gamma^{(1)}(\rho u_\gamma) \tag{B15}$$

$$= \partial_\gamma^{(1)}(\rho u_\alpha u_\beta u_\gamma) - \partial_\gamma^{(1)} D_{\alpha\beta\gamma}^{eq} + \rho c_s^2 \partial_\beta^{(1)}(u_\alpha) + \rho c_s^2 \partial_\alpha^{(1)}(u_\beta)$$
$$+ u_\alpha \partial_\beta^{(1)}(\rho c_s^2) + u_\beta \partial_\alpha^{(1)}(\rho c_s^2) - \delta_{\alpha\beta} \partial_t^{(1)}(\rho c_s^2). \tag{B16}$$

Finally,

$$\begin{aligned}\partial_t^{(2)}(\rho u_\alpha) - \partial_\beta^{(1)}\Big\{(1-\frac{\Delta t}{2\tau})\tau[\rho c_s^2(\partial_\alpha^{(1)}u_\beta + \partial_\beta^{(1)}u_\alpha) \\ +\delta_{\alpha\beta}\partial_t^{(1)}(p-\rho c_s^2) - u_\alpha\partial_\beta^{(1)}(p-\rho c_s^2) - u_\beta\partial_\alpha^{(1)}(p-\rho c_s^2) \\ -\partial_\gamma^{(1)}D_{\alpha\beta\gamma}^{eq} - \mathrm{Corr}_{\alpha\beta}^{(1)}]\Big\} = 0.\end{aligned} \tag{B17}$$

To reduce this term to the divergence of the viscous stress, one sets $\mathrm{Corr}_{\alpha\beta}^{(1)} = \delta_{\alpha\beta}\partial_t^{(1)}(p - \rho c_s^2) - u_\alpha\partial_\beta^{(1)}(p-\rho c_s^2) - u_\beta\partial_\alpha^{(1)}(p-\rho c_s^2) - \partial_\gamma^{(1)}D_{\alpha\beta\gamma}^{eq}$. By gathering the equations at $O\left(\epsilon^1\right)$ and $O\left(\epsilon^2\right)$ and multiplying each order by ϵ and ϵ^2 respectively, one eventually obtains

$$\partial_t\rho + \partial_\alpha(\rho u_\alpha) = 0 \tag{B18}$$

$$\partial_t(\rho u_\alpha) + \partial_\beta(\rho u_\alpha u_\beta + p\delta_{\alpha\beta}) = \partial_\beta\left[(\tau - \frac{\Delta t}{2})\rho c_s^2(\partial_\alpha u_\beta + \partial_\beta u_\alpha)\right] \tag{B19}$$

These are the Navier-Stokes equations where the dynamic viscosity reads

$$\mu = (\tau - \frac{\Delta t}{2})\rho c_s^2. \tag{B20}$$

To satisfy the Stokes hypothesis, i.e. a null bulk viscosity or, equivalently, a deviatoric (traceless) viscous stress, another term is finally added in the correction term so that

$$\begin{aligned}\mathrm{Corr}_{\alpha\beta} = \quad & \delta_{\alpha\beta}\partial_t(p-\rho c_s^2) \\ & - u_\alpha\partial_\beta(p-\rho c_s^2) - u_\beta\partial_\alpha(p-\rho c_s^2) \\ & - \partial_\gamma D_{\alpha\beta\gamma}^{eq} \\ & + \delta_{\alpha\beta}\frac{2}{D}\rho c_s^2\partial_\gamma u_\gamma\end{aligned} \tag{B21}$$

where D is the space dimension, and by assuming $\partial_t \approx \epsilon\partial_t^{(1)} + O(\epsilon^2)$.

ACKNOWLEDGMENTS

This work was granted access to the HPC resources of PMCS2I (Pôle de Modélisation et de Calcul en Sciences de l'Ingénieur de l'Information) at École Centrale de Lyon, Écully, France. This project benefited from computer and storage resources by GENCI at CINES thanks to the grant 2023-AD012A14929 on the MI250x partition of the supercomputer Adastra.

DATA AVAILABILITY

The data that support the findings of this study are available from the corresponding author upon reasonable request.

[1] A. Guardone, P. Colonna, M. Pini, and A. Spinelli, "Nonideal compressible fluid dynamics of dense vapors and supercritical fluids," Annual Review of Fluid Mechanics **56**, 241–269 (2024).
[2] P. A. Thompson, "A fundamental derivative in gasdynamics," The Physics of Fluids **14**, 1843–1849 (1971).
[3] W. D. Hayes, "D. the basic theory of gasdynamic discontinuities," in *Fundamentals of Gas Dynamics* (Princeton University Press, 1958) p. 416–481.

[4]M. S. Cramer, "Nonclassical dynamics of classical gases," in *Nonlinear Waves in Real Fluids* (Springer Vienna, 1991) p. 91–145.
[5]H. A. Bethe, "On the theory of shock waves for an arbitrary equation of state," in *Classic Papers in Shock Compression Science* (Springer New York, 1998) p. 421–495.
[6]Y. B. Zel'Dovich, "On the possibility of rarefaction shock waves," in *Selected Works of Yakov Borisovich Zeldovich, Volume I: Chemical Physics and Hydrodynamics*, edited by R. A. Sunyaev (Princeton University Press, 1992) pp. 152–154.
[7]M. S. Cramer and A. Kluwick, "On the propagation of waves exhibiting both positive and negative nonlinearity," Journal of Fluid Mechanics **142**, 9–37 (1984).
[8]R. Menikoff and B. J. Plohr, "The riemann problem for fluid flow of real materials," Reviews of Modern Physics **61**, 75–130 (1989).
[9]Z. Rusak and C.-W. Wang, "Transonic flow of dense gases around an airfoil with a parabolic nose," Journal of Fluid Mechanics **346**, 1–21 (1997).
[10]C.-W. Wang and Z. Rusak, "Numerical studies of transonic bzt gas flows around thin airfoils," Journal of Fluid Mechanics **396**, 109–141 (1999).
[11]P. M. Congedo, C. Corre, and P. Cinnella, "Airfoil shape optimization for transonic flows Bethe-Zel'dovich-Thompson fluids," AIAA Journal **45**, 1303–1316 (2007).
[12]P. Congedo, C. Corre, and P. Cinnella, "Numerical investigation of dense-gas effects in turbomachinery," Computers & Fluids **49**, 290–301 (2011).
[13]M. S. Cramer and A. B. Crickenberger, "The dissipative structure of shock waves in dense gases," Journal of Fluid Mechanics **223**, 325 (1991).
[14]M. S. Cramer and S. Park, "On the suppression of shock-induced separation in Bethe–Zel'dovich–Thompson fluids," Journal of Fluid Mechanics **393**, 1–21 (1999).
[15]S. H. Fergason, T. L. Ho, B. M. Argrow, and G. Emanuel, "Theory for producing a single-phase rarefaction shock wave in a shock tube," Journal of Fluid Mechanics **445**, 37–54 (2001).
[16]A. Kluwick, "Internal flows of dense gases," Acta Mechanica **169**, 123–143 (2004).
[17]P. CINNELLA and P. M. CONGEDO, "Inviscid and viscous aerodynamics of dense gases," Journal of Fluid Mechanics **580**, 179–217 (2007).
[18]S. Vitale, T. A. Albring, M. Pini, N. R. Gauger, and P. Colonna, "Fully turbulent discrete adjoint solver for non-ideal compressible flow applications." Journal of the Global Power and Propulsion Society **1**, 252–270 (2017).
[19]A. Rubino, P. Colonna, and M. Pini, "Adjoint-based unsteady optimization of turbomachinery operating with nonideal compressible flows," Journal of Propulsion and Power **37**, 910–918 (2021).
[20]N. Razaaly, G. Persico, and P. M. Congedo, "Impact of geometric, operational, and model uncertainties on the non-ideal flow through a supersonic orc turbine cascade," Energy **169**, 213–227 (2019).
[21]P. Cinnella and S. Hercus, "Robust optimization of dense gas flows under uncertain operating conditions," Computers & Fluids **39**, 1893–1908 (2010).
[22]L. Sciacovelli, P. Cinnella, and F. Grasso, "Small-scale dynamics of dense gas compressible homogeneous isotropic turbulence," Journal of Fluid Mechanics **825**, 515–549 (2017).
[23]A. Vadrot, A. Giauque, and C. Corre, "Direct numerical simulations of temporal compressible mixing layers in a Bethe–Zel'dovich–Thompson dense gas: influence of the convective mach number," Journal of Fluid Mechanics **922** (2021), 10.1017/jfm.2021.511.
[24]A. Giauque, D. Schuster, and C. Corre, "High-fidelity numerical investigation of a real gas annular cascade with experimental validation," Physics of Fluids **35** (2023), 10.1063/5.0174230.
[25]A. S. Ghate, G.-D. Stich, G. K. Kenway, J. A. Housman, and C. C. Kiris, "A wall-modeled les perspective for the high lift common research model using lava," in *AIAA AVIATION 2022 Forum* (American Institute of Aeronautics and Astronautics, 2022).
[26]E. Manoha and B. Caruelle, "Summary of the lagoon solutions from the benchmark problems for airframe noise computations-iii workshop," in *21st AIAA/CEAS Aeroacoustics Conference* (American Institute of Aeronautics and Astronautics, 2015).
[27]M. F. Barad, J. G. Kocheemoolayil, and C. C. Kiris, "Lattice Boltzmann and Navier-Stokes cartesian cfd approaches for airframe noise predictions," in *23rd AIAA Computational Fluid Dynamics Conference* (American Institute of Aeronautics and Astronautics, 2017).
[28]Y. Hou, D. Angland, A. Sengissen, and A. Scotto, "Lattice-Boltzmann and Navier-Stokes simulations of the partially dressed, cavity-closed nose landing gear benchmark case," in *25th AIAA/CEAS Aeroacoustics Conference* (American Institute of Aeronautics and Astronautics, 2019).
[29]C. L. Rumsey, J. P. Slotnick, and A. J. Sclafani, "Overview and summary of the third aiaa high lift prediction workshop," Journal of Aircraft **56**, 621–644 (2019).
[30]C. C. Kiris, A. S. Ghate, O. M. F. Browne, J. Slotnick, and J. Larsson, "Hlpw-4: Wall-modeled large-eddy simulation and lattice–Boltzmann technology focus group workshop summary," Journal of Aircraft **60**, 1118–1140 (2023).
[31]M. Aultman, Z. Wang, R. Auza-Gutierrez, and L. Duan, "Evaluation of cfd methodologies for prediction of flows around simplified and complex automotive models," Computers & Fluids **236**, 105297 (2022).
[32]P. Boivin, M. Tayyab, and S. Zhao, "Benchmarking a lattice-Boltzmann solver for reactive flows: Is the method worth the effort for combustion?" Physics of Fluids **33** (2021), 10.1063/5.0057352.
[33]D. Casalino, F. Avallone, I. Gonzalez-Martino, and D. Ragni, "Aeroacoustic study of a wavy stator leading edge in a realistic fan/ogv stage," Journal of Sound and Vibration **442**, 138–154 (2019).

[34]M. Daroukh, T. Le Garrec, and C. Polacsek, "Low-speed turbofan aerodynamic and acoustic prediction with an isothermal lattice Boltzmann method," AIAA Journal **60**, 1152–1170 (2022).
[35]M. Buszyk, C. Polacsek, T. Le Garrec, R. Barrier, E. Salze, and J. Marjono, "Aeroacoustic performances of the ecl5 uhbr turbofan model with serrated ogvs: Design, predictions and comparisons with measurements," in *30th AIAA/CEAS Aeroacoustics Conference (2024)* (American Institute of Aeronautics and Astronautics, 2024).
[36]J. Hardy, Y. Pomeau, and O. de Pazzis, "Time evolution of a two-dimensional model system. i. invariant states and time correlation functions," Journal of Mathematical Physics **14**, 1746–1759 (1973).
[37]Y. H. Qian, D. D'Humières, and P. Lallemand, "Lattice bgk models for Navier-Stokes equation," Europhysics Letters (EPL) **17**, 479–484 (1992).
[38]H. Chen, S. Chen, and W. H. Matthaeus, "Recovery of the Navier-Stokes equations using a lattice-gas Boltzmann method," Physical Review A **45**, R5339–R5342 (1992).
[39]C. Shu and N. Phan-Thien, "Special issue on the lattice Boltzmann method," Physics of Fluids **34**, 100401 (2022).
[40]X. Shan, X.-F. Yuan, and H. Chen, "Kinetic theory representation of hydrodynamics: a way beyond the navier–stokes equation," Journal of Fluid Mechanics **550**, 413 (2006).
[41]P. C. Philippi, L. A. Hegele, L. O. E. dos Santos, and R. Surmas, "From the continuous to the lattice Boltzmann equation: The discretization problem and thermal models," Physical Review E **73** (2006), 10.1103/physreve.73.056702.
[42]N. Frapolli, S. S. Chikatamarla, and I. V. Karlin, "Entropic lattice Boltzmann model for compressible flows," Physical Review E **92** (2015), 10.1103/physreve.92.061301.
[43]C. Coreixas, G. Wissocq, G. Puigt, J.-F. Boussuge, and P. Sagaut, "Recursive regularization step for high-order lattice Boltzmann methods," Physical Review E **96** (2017), 10.1103/physreve.96.033306.
[44]J. Latt, C. Coreixas, J. Beny, and A. Parmigiani, "Efficient supersonic flow simulations using lattice Boltzmann methods based on numerical equilibria," Philosophical Transactions of the Royal Society A: Mathematical, Physical and Engineering Sciences **378**, 20190559 (2020).
[45]G. Wissocq, P. Sagaut, and J.-F. Boussuge, "An extended spectral analysis of the lattice Boltzmann method: modal interactions and stability issues," Journal of Computational Physics **380**, 311–333 (2019).
[46]Y. Feng, P. Boivin, J. Jacob, and P. Sagaut, "Hybrid recursive regularized thermal lattice Boltzmann model for high subsonic compressible flows," Journal of Computational Physics **394**, 82–99 (2019).
[47]S. Hosseini and I. Karlin, "Lattice Boltzmann for non-ideal fluids: Fundamentals and practice," Physics Reports **1030**, 1–137 (2023).
[48]D.-Y. Peng and D. B. Robinson, "A new two-constant equation of state," Industrial & Engineering Chemistry Fundamentals **15**, 59–64 (1976).
[49]T. H. Chung, M. Ajlan, L. L. Lee, and K. E. Starling, "Generalized multiparameter correlation for nonpolar and polar fluid transport properties," Industrial & Engineering Chemistry Research **27**, 671–679 (1988).
[50]L. Vienne, S. Marié, and F. Grasso, "Lattice Boltzmann method for miscible gases: A forcing-term approach," Physical Review E **100** (2019), 10.1103/physreve.100.023309.
[51]L. Vienne and S. Marié, "Lattice Boltzmann study of miscible viscous fingering for binary and ternary mixtures," Physical Review Fluids **6** (2021), 10.1103/physrevfluids.6.053904.
[52]R. Foldes, E. Lévêque, R. Marino, E. Pietropaolo, A. De Rosis, D. Telloni, and F. Feraco, "Efficient kinetic lattice Boltzmann simulation of three-dimensional hall-mhd turbulence," Journal of Plasma Physics **89** (2023), 10.1017/s0022377823000697.
[53]S. A. Hosseini, P. Boivin, D. Thévenin, and I. Karlin, "Lattice Boltzmann methods for combustion applications," Progress in Energy and Combustion Science **102**, 101140 (2024).
[54]B. Dorschner, F. Bösch, and I. Karlin, "Particles on demand for kinetic theory," Physical Review Letters **121** (2018), 10.1103/physrevlett.121.130602.
[55]D. Wilde, A. Krämer, D. Reith, and H. Foysi, "Semi-lagrangian lattice Boltzmann method for compressible flows," Physical Review E **101** (2020), 10.1103/physreve.101.053306.
[56]E. Reyhanian, B. Dorschner, and I. Karlin, "Kinetic simulations of compressible non-ideal fluids: From supercritical flows to phase-change and exotic behavior," Computation **9**, 13 (2021).
[57]Z. Guo, C. Zheng, B. Shi, and T. S. Zhao, "Thermal lattice Boltzmann equation for low mach number flows: Decoupling model," Physical Review E **75** (2007), 10.1103/physreve.75.036704.
[58]Q. Li, Y. L. He, Y. Wang, and W. Q. Tao, "Coupled double-distribution-function lattice Boltzmann method for the compressible Navier-Stokes equations," Physical Review E **76** (2007), 10.1103/physreve.76.056705.
[59]G. Farag, T. Coratger, G. Wissocq, S. Zhao, P. Boivin, and P. Sagaut, "A unified hybrid lattice-Boltzmann method for compressible flows: Bridging between pressure-based and density-based methods," Physics of Fluids **33** (2021), 10.1063/5.0057407.
[60]G. Wissocq, T. Coratger, G. Farag, S. Zhao, P. Boivin, and P. Sagaut, "Restoring the conservativity of characteristic-based segregated models: Application to the hybrid lattice Boltzmann method," Physics of Fluids **34** (2022), 10.1063/5.0083377.
[61]G. Wissocq, S. Taileb, S. Zhao, and P. Boivin, "A hybrid lattice Boltzmann method for gaseous detonations," Journal of Computational Physics **494**, 112525 (2023).
[62]S. Guo and Y. Feng, "Hybrid compressible lattice Boltzmann method for supersonic flows with strong discontinuities," Physics of Fluids **36** (2024), 10.1063/5.0221289.

[63]E. Reyhanian, B. Dorschner, and I. V. Karlin, "Thermokinetic lattice Boltzmann model of nonideal fluids," Physical Review E **102** (2020), 10.1103/physreve.102.020103.
[64]X. Shan and X. He, "Discretization of the velocity space in the solution of the Boltzmann equation," Physical Review Letters **80**, 65–68 (1998).
[65]S. Guo, Y. Feng, and P. Sagaut, "Improved standard thermal lattice Boltzmann model with hybrid recursive regularization for compressible laminar and turbulent flows," Physics of Fluids **32** (2020), 10.1063/5.0033364.
[66]B. J. Palmer and D. R. Rector, "Lattice Boltzmann algorithm for simulating thermal flow in compressible fluids," Journal of Computational Physics **161**, 1–20 (2000).
[67]T. Lafarge, P. Boivin, N. Odier, and B. Cuenot, "Improved color-gradient method for lattice Boltzmann modeling of two-phase flows," Physics of Fluids **33**, 082110 (2021).
[68]C. Coreixas, B. Chopard, and J. Latt, "Comprehensive comparison of collision models in the lattice Boltzmann framework: Theoretical investigations," Physical Review E **100** (2019), 10.1103/physreve.100.033305.
[69]C. Coreixas, G. Wissocq, B. Chopard, and J. Latt, "Impact of collision models on the physical properties and the stability of lattice Boltzmann methods," Philosophical Transactions of the Royal Society A: Mathematical, Physical and Engineering Sciences **378**, 20190397 (2020).
[70]O. Malaspinas, "Increasing stability and accuracy of the lattice Boltzmann scheme: recursivity and regularization," (2015), 10.48550/ARXIV.1505.06900.
[71]H. Yoo, G. Wissocq, J. Jacob, J. Favier, and P. Sagaut, "Compressible lattice Boltzmann method with rotating overset grids," Physical Review E **107** (2023), 10.1103/physreve.107.045306.
[72]A. Guardone and B. M. Argrow, "Nonclassical gasdynamic region of selected fluorocarbons," Physics of Fluids **17** (2005), 10.1063/1.2131922.
[73]A. Guardone, L. Vigevano, and B. M. Argrow, "Assessment of thermodynamic models for dense gas dynamics," Physics of Fluids **16**, 3878–3887 (2004).
[74]B. M. Argrow, "Computational analysis of dense gas shock tube flow," Shock Waves **6**, 241–248 (1996).
[75]A. Guardone and L. Vigevano, "Roe linearization for the van der Waals gas," Journal of Computational Physics **175**, 50–78 (2002).
[76]N. Peng and Y. Yang, "Effects of the mach number on the evolution of vortex-surface fields in compressible Taylor-Green flows," Physical Review Fluids **3** (2018), 10.1103/physrevfluids.3.013401.
[77]D. J. Lusher and N. D. Sandham, "Assessment of low-dissipative shock-capturing schemes for the compressible Taylor-Green vortex," AIAA Journal **59**, 533–545 (2021).
[78]D. Wilde, A. Krämer, D. Reith, and H. Foysi, "High-order semi-lagrangian kinetic scheme for compressible turbulence," Physical Review E **104** (2021), 10.1103/physreve.104.025301.
[79]L. Sciacovelli, P. Cinnella, C. Content, and F. Grasso, "Dense gas effects in inviscid homogeneous isotropic turbulence," Journal of Fluid Mechanics **800**, 140–179 (2016).
[80]A. Giauque, C. Corre, and A. Vadrot, "Direct numerical simulations of forced homogeneous isotropic turbulence in a dense gas," Journal of Turbulence **21**, 186–208 (2020).